International Forum on Aeroelasticity and Structural Dynamics
IFASD 2024
17–21 June 2024, The Hague, Netherlands

EXPERIMENTAL VALIDATION OF STRAIN-LOAD NEURAL NETWORK MODEL ON A SLENDER HYPERSONIC VEHICLE

Ana C. Meinicke[1], Carlos E. S. Cesnik[1], Brianna L. Blocher[2], Aditya Panigrahi[2], Jayant Sirohi[2], Noel T. Clemens[2]

[1]University of Michigan
Ann Arbor, Michigan, USA
meinicke@umich.edu
cesnik@umich.edu

[2]Department of Aerospace Engineering and Engineering Mechanics, The University of Texas at Austin
Austin, TX, 78712, USA
bblocher@utexas.edu
aditya.panigrahi@austin.utexas.edu
sirohi@utexas.edu
clemens@mail.utexas.edu

Keywords: Neural network, hypersonic, inverse model, loads

Abstract: Recovery of in-flight loads is crucial for guidance, navigation, and control. The harsh aerothermal conditions experienced in hypersonic flight provide additional challenges for conventional sensors typically installed on the outer surface of the structure. This study investigates a novel vehicle-as-a-sensor concept, where internal measurements of the vehicle's deformed state are used to infer the loading it is subjected to. The proposed inverse model for this problem consists of a neural network, where strain measured through fiber optic sensors characterizes the deformed state and is used as an input to the machine learning algorithm which outputs the load state. An experimental testbed consisting of an aluminum scaled representative version of the IC3X, a slender hypersonic vehicle, is used as a proof of concept. A finite element model is developed and verified against results of a ground vibration test. The testbed is instrumented with fiber optic strain sensors along the length of the vehicle and force is applied through four actuators attached to load cells. Several static loading cases consisting of combinations of the various actuators are used to evaluate discrepancies between the as-built structure's response and the predictions from the model. Calibration factors are applied to the model strain results to account for manufacturing of the aluminum model and sensor installation uncertainties, such as thickness of the adhesive layer used to attach the optical fibers to the model surface. The neural network is trained with data consisting of numerical load and strain pairs under conditions spanning those of the experiment. The neural network-based inverse model is validated against the experimental data and compared with a Data-Driven Force Reconstruction method that assumes a linear relation between strain and force. Errors on load recovery given the strain measurements are quantified.

1 INTRODUCTION

Having reliable real-time flight data is necessary for the control of any type of aircraft. For hypersonic flight, where outer surface temperatures are expected to reach around 1400°C due to heating [1], the use of conventional surface sensors becomes a challenge. As part of a larger

AFOSR-funded University Leadership Initiative project called Full-Airframe Sensing Technology for Hypersonic Aerodynamics Measurements (FAST), a novel vehicle-as-a-sensor concept [2] is explored. This nonintrusive technique aims to infer the external aerodynamic loads on a vehicle from measurements of deformation, acceleration, and temperature on its internal structure.

Previous work by Pham et al. [2] showed the feasibility of this concept by applying machine learning to obtain pressure loads on a vehicle in hypersonic conditions using strain values. Panigrahi et al. [3] developed an alternate predictive model based on a pseudo-inverse matrix technique for estimating bending loads within structural systems and validated it with experimental data on a scaled benchtop model of a hypersonic slender vehicle.

Blocher et al. [4] obtained static pressure and temperature field measurements of a scaled model of the IC3X [5], a representative hypersonic vehicle, under angle of attack of 0° and 6° in Mach 5 flow. Similarly, Dhanagopal et al. obtained experimental pressure [6] and temperature distributions [7] of a scaled model of the IC3X in Mach 7 flow. These results were obtained to support validation efforts of the vehicle-as-a-sensor concept.

Physics-informed neural networks used to model inverse problems have previously been introduced by Raissi et al. [8] and successfully applied by Singh and Willcox [9], where they demonstrated the capability of performing trajectory adjustments of a vehicle according to onboard sensor measurements. While other inverse model methodologies are available and have been applied to the current problem of interest (see [2, 3] and [10]), neural networks (NN) are a promising solution for this problem given their capability of modeling non-linearities, quick response once trained, and extensive literature and documentation. For instance, Klotz et al. [11] demonstrated that a neural network can be trained on experimental strain data measured with a fiber optic sensing system on a modern business jet wing and is able to successfully recover wing twist angle.

A strain-to-load neural network model is developed for a scaled version of the IC3X and validated with experimental data. Considerations on the accuracy of load recovery are provided, given the sensor locations and noise levels observed on the experimental setup.

The models used for this analysis are described in Section 2, where the experimental setup and equipment is discussed followed by a description of the numerical model used for generating the training data. Given that a numerical model is always an approximation of the reality, a methodology for calibrating the data is proposed. Section 3 describes the process for obtaining the inverse model and details on the neural network architecture definition. The results are shown in Section 3.3, where the errors on model calibration and load recovery are quantified. Finally, Section 4 describes the main conclusions.

2 MODELS AND METHODS

The experimental validation of the proposed NN-based inverse model requires the setup of a representative testbed and the development of an accurate numerical model for the generation of training data. For simplification, the current setup consists of a no-flow benchtop model. And for the possibility of including thermal effects in continuing studies the current model is made of aluminum as opposed to ABS, as was previously developed and used by Panigrahi et al. [12]. This change in material ensures that the model can be heated without melting or plastically deforming.

2.1 Experimental Model and Setup

The model was a 40% scale of the full-size IC3X, and was machined from Aluminum 6061 with a Young's Modulus of 71 GPa. The internal structure was designed to have localized areas of thinner wall, referred to as flexures in Figure 1. These flexures created areas of higher strain and produced ideal strain sensor location points. The model was supported by a sting balance approximately 0.42 meters away from the tail, serving as the model's fixed boundary condition.

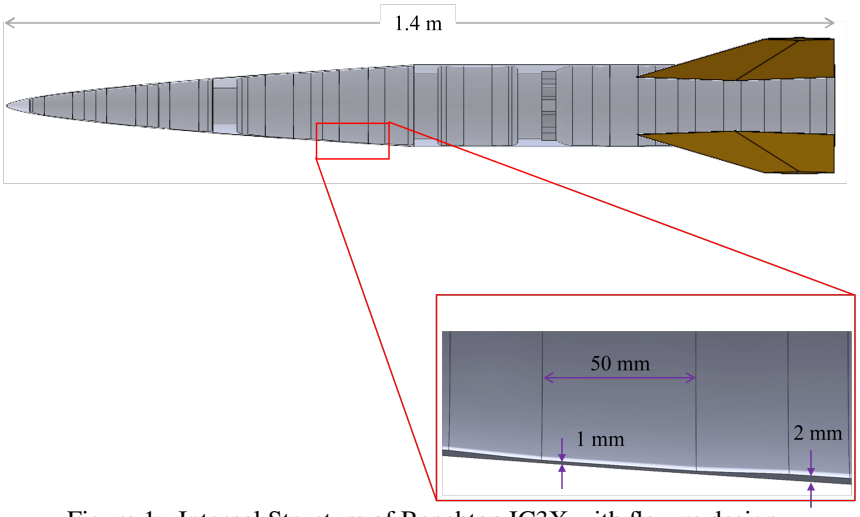

Figure 1: Internal Structure of Benchtop IC3X with flexure design.

Four linear actuators were attached to the underside of the model, shown in Figure 2, with three actuators connected forward of the sting attachment, and one actuator attached aft of the sting attachment. Each actuator sat in-line with a ball joint to account for angular deflection of the model and keep the applied force normal to the surface. It also sat in-line with a LCM201 Tension/Compression load cell capable of up to 500 Newton loading with a $\pm 1\%$ Full-Scale Output accuracy. Its signal was acquired in an internal full-bridge configuration with the NITB-4330 8-Channel Bridge Input module mounted in a PXIe-1088 chassis.

Four fiber optic strands were mounted inside the model, each containing eight Fiber Bragg Grating (FBG) sensors that measured local bending strain. The sensors were attached to the model using Micro Measurements M-Bond 200 Adhesive to allow for strain transmittance. The fiber cables were connected to the Technobis Switched Gator FBG Interrogator that emitted a Class 1 laser along each strand at a defined length of time per channel. The Switched Gator measured the reflected wavelength from each FBG sensor before it switched to the next channel, and a change in the reflected wavelength would correspond to an induced strain. The Switched Gator operated in a "switched" configuration where the laser was gated through each connected channel one at a time, and data was acquired in that time frame. The configuration used for this setup allowed for 50 milliseconds of data collection per channel switch, obtaining approximately 900 samples at each interrogation. From there, five of these chunks of samples were used in later averaging to obtain a single strain value per sensor.

The sensors were mounted in the centers of flexures, near the sting attachment point, and in the tail section, shown in the schematic in Figure 2. Fore of the attachment point, sensors were placed 30-degrees off from the cardinal directions, allowing all sensors to measure appreciable strain and avoid low-to-no microstrain response at/near the neutral axis. Aft of the attachment, the sensors were placed at the 0/90/180/270-degree locations. Two sensors in the tail region were unresponsive, but thirty sensors remained operational. The FBG sensors were capable of

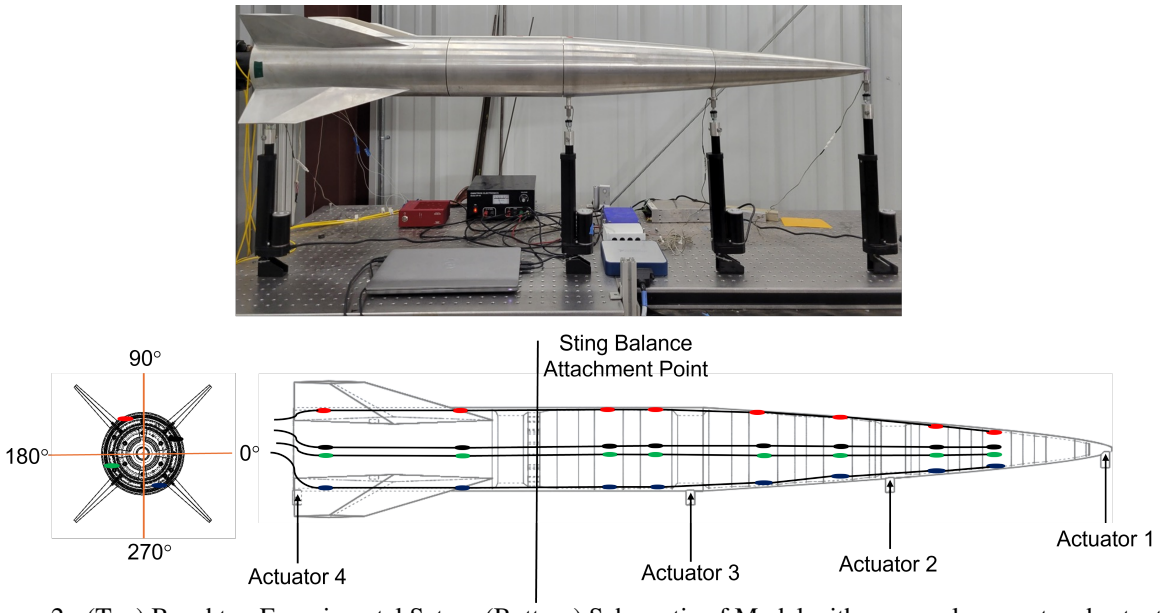

Figure 2: (Top) Benchtop Experimental Setup. (Bottom) Schematic of Model with sensor placement and actuator locations. Red - 30° from Model's 90°, Blue - 30° from Model's 270°, Black - 30° from Model's 180°, Green - 30° from Model's 0°.

measurement with noise ranging approximately 6 microstrain with a standard deviation of 2 microstrain.

Impact hammer testing was conducted to experimentally identify the modal frequencies of the benchtop model. The model was suspended via bungee cords at the nose and tail to allow a free-free boundary condition. A PCB Piezotronics single-axis shear accelerometer was mounted to the model to measure the response after a hammer impact, and the hammer struck the model in eleven different locations. The hammer's applied force was also measured which allowed for a frequency response function (FRF) to get mode shapes and natural frequencies for each location. Two hammer location FRFs are shown in Figure 3 as well as the resulting first bending mode shape at approximately 321 Hz.

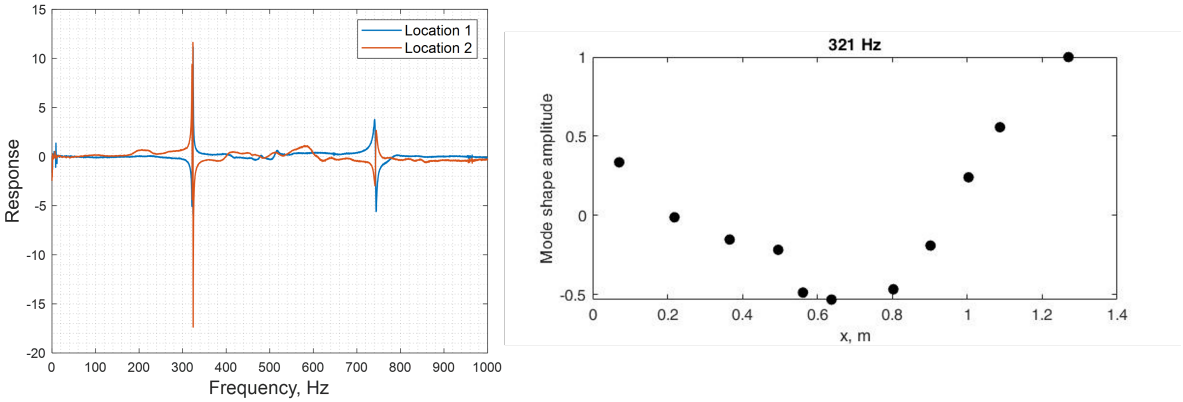

Figure 3: (Left) Frequency Response Function at two locations. (Right) First Bending Mode Shape at 321 Hz.

Thirty nine load cases were created with this experimental setup to validate the recovered forces of the inverse models. The load cases that are referred to in later sections are shown in Table 1. A positive force indicates the actuator pushing the model and travelling upward, while a

negative force indicates the actuator pulling the model and travelling downward.

Table 1: Experimental loading cases. Forces are in newtons.

Case #	F 1	F 2	F 3	F 4	Case #	F 1	F 2	F 3	F 4
1	36.6	59.5	0	0	**21**	0	-94.1	-104.5	0
2	-35.7	-54.5	0	0	**22**	35.4	35.6	12.5	0
3	109.6	12.6	0	0	**23**	-12.7	-32.5	-23.1	0
4	-89.0	-29.1	0	0	**24**	23.4	44.0	51.1	0
5	6.0	98.6	0	0	**25**	-17.8	-45.0	-39.9	0
6	-13.7	-65.9	0	0	**26**	11.7	38.1	97.4	0
7	90.7	93.0	0	0	**27**	-28.0	-37.4	-53.6	0
8	82.1	-59.8	0	0	**28**	52.7	29.6	25.1	0
9	-51.5	-81.1	0	0	**29**	-58.3	-54.2	-30.0	0
10	-88.0	141.8	0	0	**30**	72.7	84.7	56.3	0
11	84.6	-121.7	0	0	**31**	95.4	91.8	71.3	0
12	0	59.4	41.2	0	**32**	-67.8	-63.1	-71.3	0
13	0	-63.1	-39.3	0	**33**	-52.9	-79.9	-112.3	0
14	0	22.6	92.1	0	**34**	44.9	48.1	44.3	37.3
15	0	-14.3	-93.6	0	**35**	37.5	73.1	70.4	-83.4
16	0	129.8	165.9	0	**36**	-37.9	-68.6	-56.6	99.4
17	0	-109.1	-137.4	0	**37**	-46.4	-92.3	116.3	70.8
18	0	82.3	106.2	0	**38**	59.9	103.6	-109.6	-73.9
19	0	92.8	-110.7	0	**39**	-50.4	111.3	-73.5	83.0
20	0	-86.7	100.5	0					

2.2 Numerical Model and Calibration

A finite element model (FEM) of the benchtop model of the IC3X was developed in Abaqus. The geometry was meshed with 10-noded tetrahedrals, consisting of elements that are appropriate for elastic static analysis as well as thermal transient analysis. A mesh convergence analysis was performed where the relative error on displacement in selected nodes for the final mesh was lower than 0.4%. A highly refined mesh was chosen since accurate strains were the main output of interest. The material properties assigned to the model can be seen in Table 2.

Table 2: Aluminum 6061 properties.

Density	2770 $\mathrm{kg/m^3}$
Young's modulus	71 GPa
Poisson's ratio	0.33

Results from the experimental modal characterization of the model, as presented in Section 2.1, were used for the verification of the FEM. The first and second bending modes were experimentally identified, and their mode shapes were qualitatively compared to the numerical ones. The frequency comparison for the first 6 modes can be seen in Table 3, where a range of experimental frequencies is shown considering the results obtained from the eleven FRFs.

Modes 1 and 2 correspond to the first in-plane and first out-of-plane bending modes, respectively. While the as-built structure shows a difference in frequency, the numerical model does not. This difference can be attributed to the loss of axial symmetry in the experimental model due to manufacturing deviations as well as the setup of the boundary condition. Modes 3 and

Table 3: Frequency comparison between FEM and the as-built structure.

Mode	Experimental	Numerical	Difference
1	[320.99, 321.78] Hz	334.28 Hz	[3.74, 3.98] %
2	[323.35, 324.13] Hz	334.28 Hz	[3.04, 3.27] %
3	[471.78, 479.63] Hz	476.61 Hz	[−0.63, 1.01] %
4	-	560.75 Hz	-
5	[738.66, 747.09] Hz	705.33 Hz	[−4.73, −5.92] %
6	[738.66, 747.09] Hz	705.37 Hz	[−4.72, −5.91] %

4 correspond to fin dominated modes, not easily captured experimentally due to the lack of excitation on that location during the test. Modes 5 and 6 correspond to the second in-plane and out-of-plane bending modes. For these, the identification of two separate peaks on the FRFs was not possible. The differences observed range between 3 to 6%. The first bending experimental frequency is lower than the numerical one, whereas the second bending experimental frequency is higher than the numerical one.

Mass and center of gravity values were also compared, as can be seen in Table 4. The center of gravity was measured from the tail of the structure. The differences observed were all lower than 6%, showing that the numerical model is a good representation of the as-built structure.

Table 4: Mass properties comparison between FEM and the as-built structure.

	Experimental	Numerical	Difference
Mass	7.2 kg	7.6 kg	5.3%
CG	0.45 m	0.43 m	−4.6%

The measured strains according to different static loading conditions are compared against the numerically obtained strains to evaluate the necessity of calibration of the model. The differences observed can be due to:

- the attachment of the sensor to the model surface,
- wall thickness discrepancy between the as-built and numerical models close to the measurement location due to manufacturing imperfections,
- difference in position and direction of measurement of the strain between the as-built and numerical models,
- hysteresis on the experimental data due to thermal drifting of the sensor, and
- measurement noise.

The effect of hysteresis can be mitigated by zeroeing the equipment for every measured load point (essentially recalibrating it). The position and direction of the sensors were carefully measured and small differences here are not expected to be of great influence. Since the structure was CNC machined, a sufficient level of precision is expected on the wall thickness. Thus, the main contributor to the difference is expected to be the thickness of the glue used for attaching the fiber optic sensing cable to the model surface.

In order to properly account for this, a calibration factor is applied to each of the 32 sensor locations. A minimum set of loads is used on the calibration process. For this experiment, using load cases with single actuator inputs considering actuators 1 and 4 is enough, since if actuator 4 was not included there would be sensing points not excited due to the position of the boundary condition. The load cases consisted of forces ranging from −152 N to 394 N. The

calibration factor is then obtained by minimizing the error defined as

$$Error = \left| \frac{\varepsilon_{num}}{CF} - \varepsilon_{exp} \right|, \tag{1}$$

where ε_{num} corresponds to the numerical strain, CF corresponds to the calibration factor, and ε_{exp} corresponds to the experimental strain. Values of strain lower than a threshold (attributed to noise and also close to the zero value) are discarded to avoid distortions of the data. For the results presented here, this threshold was set to 5 microstrain. This method accounts for calibrating the slope of the data, given that the load to strain relation here is linear. And it ignores any biases/offsets in the experimental data, which seemed to be minimal upon observation and should be filtered out. The average calibration factor obtained is of around 1.2, while ranging from 0.8 to 1.7.

These calibration factors were verified against the load cases presented in Table 1. The error obtained for each of the strain sensors after applying the calibration factors to the numerical data can be seen in Figure 4. Most of the differences lie well within noise range, with a few outliers.

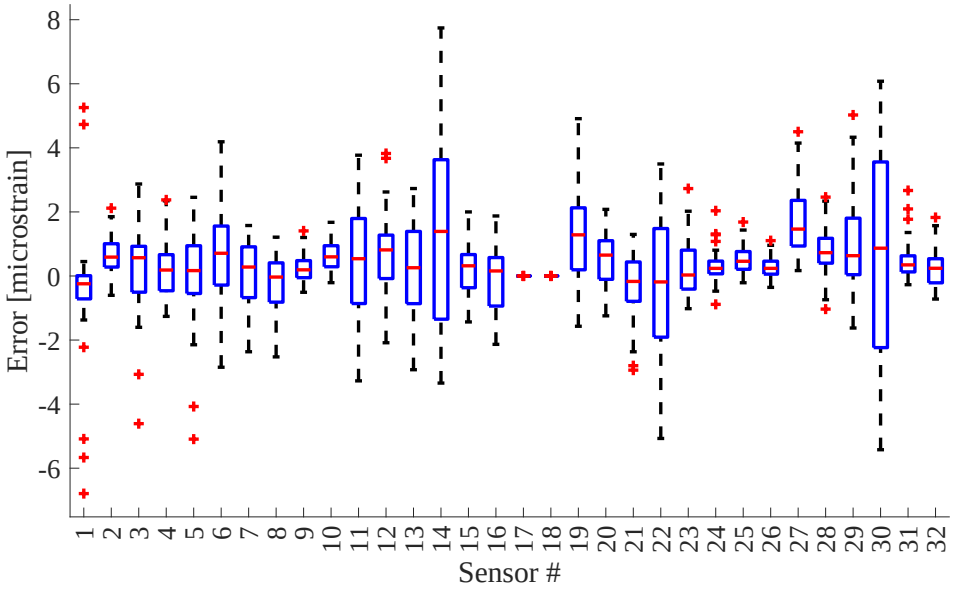

Figure 4: Error between calibrated numerical strain data and experimental strain data for the verification cases.

3 STRAIN-TO-LOAD INVERSE MODEL

The methodology for obtaining the inverse model is presented next, followed by the results of applying it to the numerical and the experimental cases. The neural network-based methodology is presented first, followed by a summary of the Data-Driven Force Reconstruction approach as applied by Panigrahi et al. [3]. Then, a comparison between both methods on force recovery is performed.

3.1 Neural Network-Based

The strain-to-load inverse model introduced here for the vehicle-as-a-sensor concept is obtained through a neural network (NN). An NN is proposed as opposed to other solutions that consider the linearity of the problem such as the inverse map developed by Pham et al. [10] and the pseudo-inverse matrix approach applied by Panigrahi et al. [3]. The application of the NN will

allow for capturing nonlinearities arising from the addition of thermal effects to be done at later studies.

The NN is trained on numerical data coming from the calibrated FEM results. The training data consist of load and strain pairs obtained with elastic static solutions. The load is modeled as four point forces positioned according to the actuators setup and the strain is obtained on the 32 sensor locations in the direction of installation. A total of 2401 cases were generated with combinations of the four actuators ranging from -300 N to 300 N in increments of 100 N.

A feedforward fully connected neural network for regression is trained. The number of layers, varying from 1 to 5, the size of each layer, varying from 1 to 400 , the activation function, the use of standardization, and the use of regularization are obtained using Bayesian optimization with a k-fold cross validation using 5 partitions. The k-fold partition allows for automatic resampling of the data, mitigating any biases on separating it between training and testing sets.

3.2 Data-Driven Force Reconstruction (DDFR)

Another approach implemented to predict forces is the Data-Driven Force Reconstruction (DDFR) method, previously applied to the IC3X by Panigrahi et al. [3]. In DDFR, a parameter called the influence coefficient matrix is calculated using the input (strain) and output (force), and that parameter itself becomes the basis for an inverse model that predicts output based on the given input. The first step was to calculate the strain influence coefficient matrix. Assuming strain and force are linear, one can relate strain ε for a given force f using Equation 2. Here $[C]$ is called the strain influence coefficient matrix.

$$\varepsilon = [C]\{f\} \tag{2}$$

The strain and force are variables that can be obtained from the experiment and, therefore, are known parameters. Since forces and strains are known, one can employ a least-square formulation to calculate $[C]$, as shown in Equation 3. After calculating the $[C]$ matrix, one can take the Moore-Penrose inverse matrix as shown in Equation 4, where the prediction of force f_p is calculated by supplying strain input ε to the pseudo-inverse of the $[C]$ matrix, denoted by $[C]^+$.

$$[C] = \{\varepsilon\}\{f\}(ff^T)^{-1} \tag{3}$$

$$\{f_p\} = (C^T C)^{-1} C^T \{\varepsilon\} = [C]^+ \{\varepsilon\} \tag{4}$$

3.3 Results

It might seem auspicious to divide the problem according to the boundary condition. That is, to have an inverse model considering the set of sensors from the nose until the clamping point to recover the forces on this side and then another inverse model considering the set of sensors from the clamping point until the tail to recover the force at the tail. While there isn't necessarily a downside of following this definition, a well-trained and well-calibrated neural network is able to pick such patterns out from the available training data.

Moreover, in the presence of faulty sensors it is best to have a neural network trained considering this possibility. Table 5 summarizes the normalized mean squared error (NMSE) obtained on load recovery with this consideration. The first configuration, called **NN1**, considers all the 32 sensors for training and evaluation. The second configuration, called **NN1 + Faulty** considers the previously trained neural network, but zeroes the input for sensors 17 and 18 since those are

faulty. The third configuration, called **NN2**, is a neural network trained with additional training data where the added data consist of repeating the previous set but with sensor 17 zeroed, and then repeating it once more with sensor 18 zeroed, and considers all the 32 sensors working for evaluation. The fourth configuration, called **NN2 + Faulty**, considers the previously trained neural network, but zeroes the input for sensors 17 and 18. For these cases all trained neural networks presented a coefficient of determination (R^2) of 1.

Table 5: Comparison of error on load recovery of NN-based inverse models considering faulty sensors.

	NN1	**NN1 + Faulty**	**NN2**	**NN2 + Faulty**
NMSE	9.1×10^{-5}	4.9×10^{-2}	3.4×10^{-6}	3.4×10^{-6}

This error is obtained considering numerical data only for the 39 conditions presented in Table 1 – which were not used to generate the training data – and normalized by the maximum target value. Differences between **NN1** and **NN1 + Faulty** are due to inserting values of zero in sensors 17 and 18 on the NN trained with all 32 sensors. It is possible to see that there is a considerable change in the order of the magnitude of the error. Differences between **NN2** and **NN2 + Faulty** are negligible. Now, comparing **NN1** and **NN2**, **NN2** results in lower error. This is likely due to **NN2** being trained on a larger number of training data cases.

Random noise modeled as a normal distribution is applied to the numerical data in order to evaluate how sensitive the recovery of the forces is to noise. The NMSE according to noise level can be seen in Fig. 5 (note that the error is represented in a logarithmic scale).

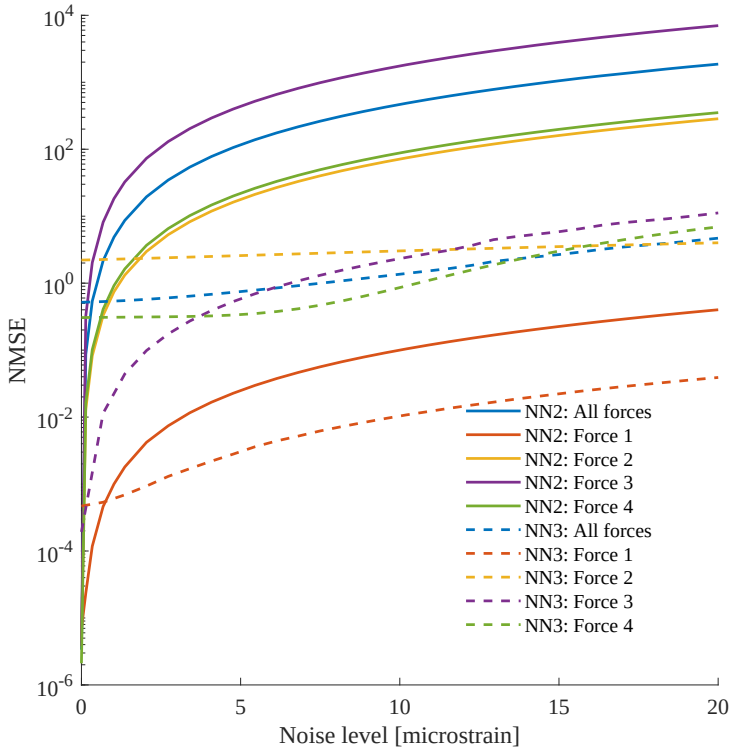

Figure 5: Normalized mean squared error according to noise level on the recovery of forces through the inverse model, where dashed lines indicate the use of training data with synthetic noise (**NN3**).

The inverse model is very sensitive to noise, especially around the 0 to 5 microstrain region. Also, whereas Force 1 can be recovered with a low level of error for all noise levels considered,

recovery of Force 3 tends to be more inaccurate. This indicates that there might not be enough sensor points for the inverse model to accurately recover Force 3 (there are only 8 sensor points between the clamping point and the point of application for Force 3).

The signal-to-noise ratio can also be contributing to a larger error in recovery of Force 3. However, if that were the main contributor the error would be increasing more rapidly as the noise level increases. And, by observation, the strain values measured close to Force 3 are of the same order of magnitude as those observed close to Force 1.

Another solution to this issue consists of artificially adding noise to the training data. Assuming a normal distribution for noise, with no bias and noise levels within 5 microstrain, five sets of random noise where added to the training data. The results for this NN trained with synthetic noise (called **NN3**) can also be seen in Figure 5.

It is clear that it is possible to improve the accuracy in load recovery for all forces with adding artificial noise to the training data. While if 0 noise is considered the recovery of the forces is less accurate, when noise is considered, as is expected in any measurement, the overall error is decreased.

The low values of error observed when no noise is considered (**NN2** at 0 noise level) indicate that the sampling chosen to generate the training data is adequate for the recovery of the forces for the 39 cases considered for this evaluation.

However, the error increases for **NN3**, that is, when noise is considered in the training data. This increase in error is related to the signal-to-noise ratio observed in the verification cases. The NMSE according to signal-to-noise ratio observed in those cases can be seen in Figure 6. While all the cases considered present a signal-to-noise ratio of at least 2/1, where the signal is the maximum absolute value of strain measured considering all 32 sensors and the noise level is of 6 microstrain, only 5 cases present a signal-to-noise ratio of 10/1. The ratio between NMSE of **NN3** over the NMSE of **NN2** is used to decrease any bias in the trend due to which cases are being considered in the evaluation, and the ratio is normalized to its initial value to simplify the interpretation of the results. It can be seen that generally there is a considerable decrease in the NMSE as a higher signal-to-noise ratio is observed.

All previous results are obtained with numerical data only. When experimental strain is used as the input for **NN3**, the recovery of the forces can be seen compared to their expected value and results obtained with Panigrahi et al.'s DDFR method [3] in Figure 7.

While recovery of Force 1 is successful, recovery of the other forces seems more challenging. Their accuracy could be further improved by:

- obtaining experimental data with higher signal-to-noise ratio,
- improving the calibration of the numerical data,
- adding different noise levels to the training data set,
- using a noise distribution closer to what is observed during the experiment for generating the artificial noise added to the training data, and
- adding more sensor points.

When comparing with Panigrahi et al.'s DDFR technique [3], the NN is less accurate for Force 2, while more accurate for Forces 1, 3, and 4, especially in cases where the force is zero. It

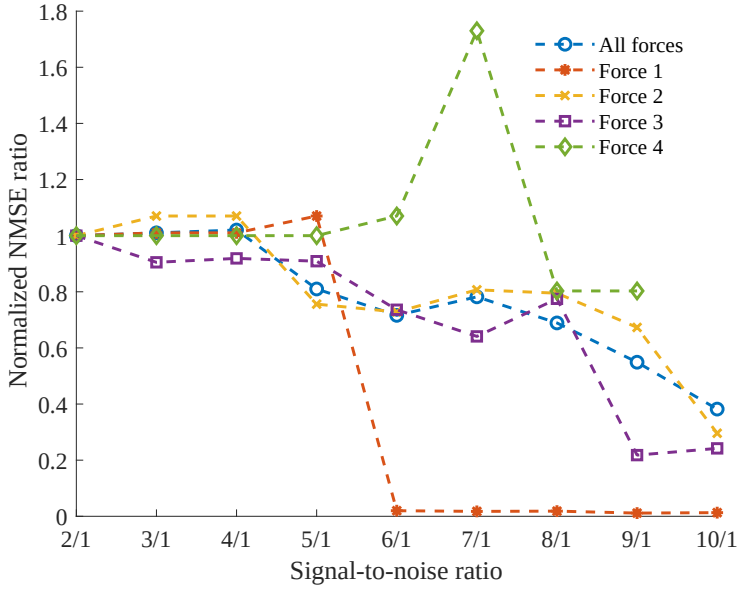

Figure 6: Signal-to-noise ratio versus normalized NMSE ratio between **NN3** and **NN2**.

seems that the NN is better able to handle the noise, while losing some of the accuracy on higher loads due to that. Table 6 compares the mean absolute difference of both inverse models with the experimental data.

Table 6: Comparison of mean absolute difference between **NN3** and DDFR recovered forces against experimental data.

NN3				*DDFR*			
Force 1	**Force 2**	**Force 3**	**Force 4**	**Force 1**	**Force 2**	**Force 3**	**Force 4**
0.01 N	8.55 N	4.51 N	0.46 N	0.21 N	2.57 N	10.38 N	0.99 N

As the next step for this work is to implement these methods on a distributed loading case (e.g. hypersonic wind tunnel pressure distribution), it is useful to compare relevant pseudo-aerodynamic terms between the recovered and experimental results. Total lift, pitching moment, and center of pressure – in this case, the location where total lift acts – defined respectively in Equations 5 to 7, were used as comparison parameters between the two methods. For brevity, only a single case from each loading configuration was listed in Table 7 showing the percent difference between recovered and experimental forces.

$$L_T = \sum_{i=1}^{4} F_i \tag{5}$$

$$M_P = \sum_{i=1}^{4} F_i x_i \tag{6}$$

$$x_{CoP} = \frac{M_P}{L_T} \tag{7}$$

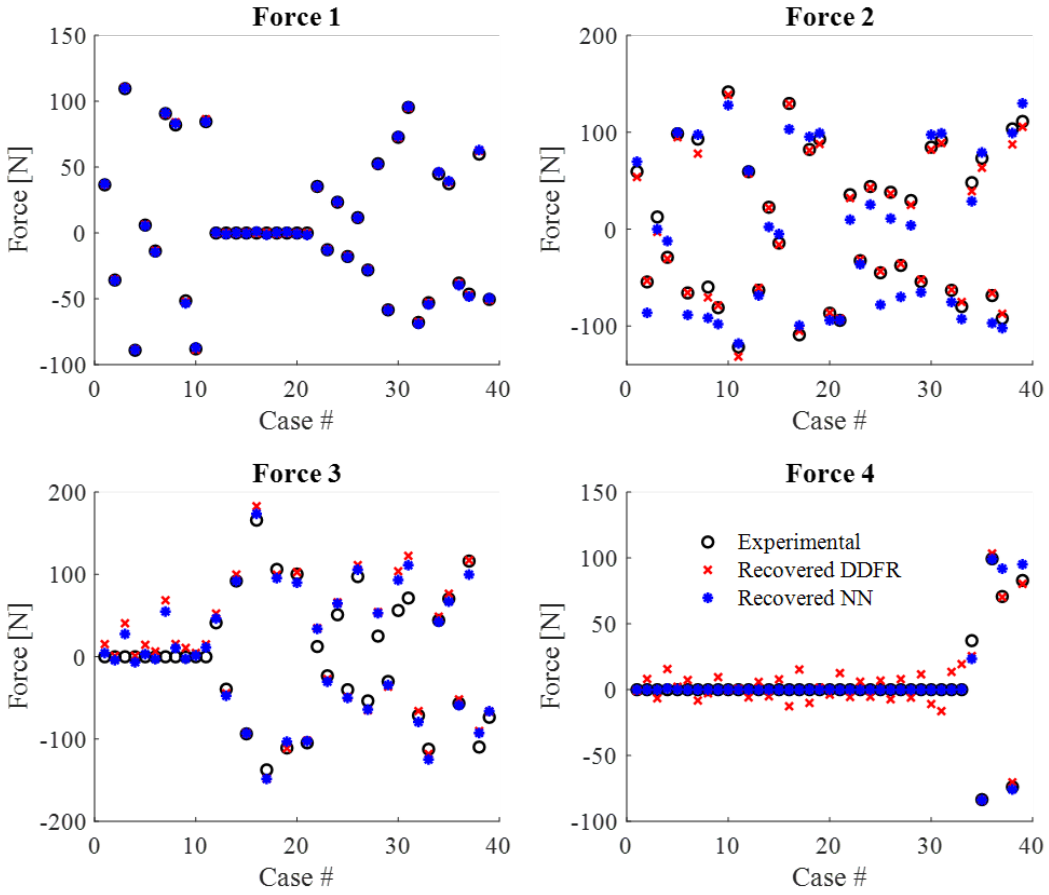

Figure 7: Recovered forces using experimental strain in **NN3** compared with experimental value and Panigrahi et al.'s DDFR [3].

Table 7: Percent difference of aerodynamic terms between recovered and experimental forces.

		NN3			*DDFR*		
Case #	**Load Configuration**	L_T	M_P	x_{CoP}	L_T	M_P	x_{CoP}
1	Force 1/Force 2	16.0	11.2	2.2	9.6	1.2	4.1
12	Force 2/Force 3	6.4	4.5	0.6	3.4	9.0	1.7
24	Force 1/Force 2/Force 3	4.2	12.8	3.4	7.1	8.2	0.4
35	Force 1/Force 2/Force 3/Force 4	4.1	3.6	0.5	2.8	2.4	0.4

Overall, the DDFR model predicted these aerodynamic terms more accurately. However, the neural network presented errors of the same order of magnitude, while resulting in a more accurate estimation of the center of pressure for some cases.

4 CONCLUDING REMARKS

An inverse model that predicts loads given strain values was developed based on a neural network and its accuracy was assessed given experimental data and compared to a pseudo-inverse based method. The neural network-based inverse model is proposed for addressing a novel vehicle-as-a-sensor concept for hypersonic flight conditions, where the vehicle's deformed state is used to infer the aerodynamic state it is subjected to.

An experimental testbed based on a scaled version of the IC3X was developed, where strain is measured through fiber optic sensing cables and four point forces are applied through actuators. The experimental results are used for validation of the proposed method.

The neural network is trained on numerical data obtained through static elastic solutions of a detailed calibrated FEM of the scaled model. The training data set was enhanced with considerations on faulty sensors and noise levels for improved accuracy on load recovery. The effect of signal-to-noise ratio on the presented results was also assessed.

While recovery of forces, as well as of aerodynamic terms, is shown to be successful for the proposed method, some challenges regarding accuracy remain. They can be tackled mainly by obtaining an adequate characterization of the noise expected in the measurements, and also considering signal-to-noise ratio conditions where the patterns to be observed in the strain measurements are not significantly changed by noise.

Future studies will include the addition of thermal effects to the problem and address the recovery of pressure distributions as measured in wind tunnel experiments.

5 ACKNOWLEDGMENTS

This work is supported by AFOSR grant FA9550-21-1-0089 under the NASA University Leadership Initiative (ULI). The authors would also like to acknowledge Marc A. Eitner for providing the GVT results used in this study.

6 REFERENCES

[1] Bowcutt, K., Finley, D., Hagseth, P., et al. (2023). Lecture Notes in Hypersonic Flight Vehicle Design and Performance Analysis - Online Short Course. AIAA.

[2] Pham, J., Morreale, B. J., Clemens, N., et al. (2022). Aerodynamic Sensing for Hypersonics via Scientific Machine Learning. In *AIAA AVIATION Forum*. doi:https://doi.org/10.2514/6.2022-3717.

[3] Panigrahi, A., Nguyen, A. Q., Eitner, M. A., et al. (2024). Strain-Data Driven Force Reconstruction Using Pseudo-Inverse Matrix. In *IMAC-XLII 2024 Conference*.

[4] Blocher, B. L., Eitner, M. A., Sirohi, J., et al. (2024). Pressure Field and Mean Deflection Estimation of a Hypersonic Vehicle Model in Mach 5 Flow. In *AIAA SCITECH 2024 Forum*. doi:https://doi.org/10.2514/6.2024-2849.

[5] Witeof, Z. D. and Neergaard, L. J. (2014). Initial Concept 3.0 Finite Element Model Definition. Tech. rep., Eglin AFB, FL.

[6] Dhanagopal, A., Williamson, C., LaLonde, E. J., et al. (2023). High-Speed Pressure Sensitive Paint Measurements of the Initial Concept 3.X Vehicle at Mach 7. In *AIAA SCITECH 2023 Forum*. doi:https://doi.org/10.2514/6.2023-1179.

[7] Dhanagopal, A., Strasser, N., Andrade, A., et al. (2024). Global Surface Temperature Distribution on the Initial Concept 3.X Vehicle at Mach 7. In *AIAA SCITECH 2024 Forum*. doi:https://doi.org/10.2514/6.2024-0668.

[8] Raissi, M., Perdikaris, P., and Karniadakis, G. E. (2019). Physics-Informed Neural Networks: A Deep Learning Framework for Solving Forward and Inverse Problems Involving

Nonlinear Partial Differential Equations. *Journal of Computational Physics*, 378, 686–707. ISSN 0021-9991. doi:https://doi.org/10.1016/j.jcp.2018.10.045.

[9] Singh, V. and Willcox, K. E. (2017). Methodology for Path Planning with Dynamic Data-Driven Flight Capability Estimation. *AIAA Journal*, 55(8), 2727–2738. doi:https://doi.org/10.2514/1.J055551.

[10] Pham, J., Ghattas, O., and Willcox, K. E. (2024). Real-Time Aerodynamic Load Estimation for Hypersonics via Strain-Based Inverse Maps. In *AIAA SCITECH 2024 Forum*. doi:https://doi.org/10.2514/6.2024-1228.

[11] Klotz, T., Pothier, R., Walch, D., et al. (2021). Prediction of the Business Jet Global 7500 Wing Deformed Shape Using Fiber Bragg Gratings and Neural Network. *Results in Engineering*, 9, 100190. ISSN 2590-1230. doi:https://doi.org/10.1016/j.rineng.2020.100190.

[12] Panigrahi, A., Blocher, B., Eitner, M., et al. (2024). Experimental Modal Analysis of an Additively Manufactured Model. In *Special Topics in Structural Dynamics & Experimental Techniques, Volume 5*. Springer Nature Switzerland. ISBN 978-3-031-37007-6, pp. 155–162.

COPYRIGHT STATEMENT